Rare Metal Materials and Engineering
Volume 55, Issue 5, May 2026
Available online at www.rmme.ac.cn

Science Press

Cite this article as: Wu Dan, Wang Gang, Shi Rongpei. Multi-physics Study of Thermal History Effect on Non-equilibrium Solidification Microstructure of Ti-Nb Alloy During Dual-Track Selective Laser Melting[J]. Rare Metal Materials and Engineering, 2026, 55(05): 1157-1169. DOI: https://doi.org/10.12442/j.issn.1002-185X.20250053.

ARTICLE

Multi-physics Study of Thermal History Effect on Non-equilibrium Solidification Microstructure of Ti-Nb Alloy During Dual-Track Selective Laser Melting

Wu Dan[1], Wang Gang[1], Shi Rongpei[2]

[1] School of Materials Science and Engineering, South China University of Technology, Guangzhou 510641, China; [2] School of Materials Science and Engineering, Harbin Institute of Technology, Shenzhen, Shenzhen 518055, China

Abstract: A multi-physics approach was used to quantify the effect of process parameters (laser power, scanning speed, hatch spacing, and scanning strategy) on the thermal history and corresponding microstructure evolution of Ti-25Nb (at%) alloy during the dual-track selective laser melting (SLM) process. Simulation results reveal that during the dual-track SLM process, increasing laser power results in greater thermal accumulation, leading to a molten pool of larger volume and coarser grains. Reducing scanning speed enhances remelting and promotes cellular growth at the top of molten pool, whereas faster scanning speed leads to rougher melt tracks and finer grains. Notably, hatch spacing significantly influences the molten pool dimensions and microstructures, and smaller hatch spacing promotes remelting. Furthermore, the orientations of grains in the second track during zigzag scanning differ markedly from those in the first track. More importantly, compared with those after the first track, both the temperature gradient and cooling rate at the boundaries of remelting molten pool are reduced after the second track scanning, resulting in slower interface velocity and significant change in solidification microstructure. This research provides a theoretical foundation for controlling non-equilibrium microstructure and offering novel insights into the optimization of SLM process parameters of titanium alloys.

Key words: selective laser melting; non-equilibrium solidification; thermal history; finite interface dissipation phase-field model; microstructure evolution

1 Introduction

Additive manufacturing (AM) technique has received significant interest in the industry due to its ability to create complex geometrical parts by layer-wise stacking of materials based on computer-generated designs[1]. This capability offers vast possibilities for lightweight design, particularly appealing in the medical and industrial fields. Among those AM techniques, selective laser melting (SLM), specifically laser powder bed fusion, is one of the most widely adopted methods for metal parts, owing to its design flexibility and ability to achieve superior mechanical properties of materials, compared with the conventional manufacture methods[2–5].

Titanium alloys are extensively used in biomedical applications due to their low elastic modulus, high specific strength, excellent biocompatibility, and good corrosion resistance[6–12]. Notably, Ti-Nb alloys possess elastic modulus that can well match that of human cortical bone (about 20 GPa), and they do not contain biologically toxic elements, such as Al and V. Moreover, an optimal Nb content can lead to good shape memory effect of the alloy, making Ti-Nb alloys primary candidates for the development of biomedical Ti-alloys of low elastic modulus. For example, Wang et al[13] examined the effects of Nb content on the properties of Ti-Nb alloys processed via SLM, and they revealed that the SLMed Ti-25Nb (at%) alloy retains a complete β-phase microstructure and exhibits a minimal elastic modulus of 18.7±1.4 GPa, thereby fulfilling the modulus requirements for cortical bone

Received date: May 25, 2025
Foundation item: Guangdong Basic and Applied Basic Research Foundation (2024A1515011873); Shenzhen Basic Research Project (JCYJ20241202123504007); Shenzhen Science and Technology Innovation Commission (KJZD20240903101400001, KJZD20240903102006009)
Corresponding author: Wang Gang, Ph. D., Associate Professor, School of Materials Science and Engineering, South China University of Technology, Guangzhou 510641, P. R. China, E-mail: msgwang@scut.edu.cn

applications.

Despite the promising potential of SLM technique for Ti-Nb alloy fabrication, numerous challenges persist, including the prevalence of defects (pores) in the printed components and the unclear mechanism governing microstructure formation and evolution[14–16]. To produce parts with superior properties, it is essential to establish the relationships among composition, process parameters, microstructure, and performance[17]. Based on the inherent complexities of SLM process, characterized by various physical and chemical phenomena (heat transfer, fluid dynamics, and solute diffusion), conducting experimental studies is complicated, costly, and time-consuming. Recently, the development of computational materials science has enabled researchers to leverage computer simulations to investigate SLM process. These simulations facilitate the exploration about the relationship between process parameters and temperature field, and their effect on microstructure and the mechanical properties of the printed parts can also be investigated, effectively selecting the optimal process parameters and providing valuable experimental guidance.

In Ref. [18], the non-equilibrium solidification of Ti-25Nb (at%) alloy during single-track SLM process was discussed. Firstly, a powder-bed computational fluid dynamics model was adopted to obtain the detailed temperature and flow fields of SLM process. Subsequently, the temperature gradient and cooling rate at various micro-regions of the stable molten pool boundary were extracted and coupled with the phase-field model. The simulation results illustrated the non-equilibrium solidification microstructure of SLMed Ti-Nb alloys, thereby establishing a quantitative relationship between process parameters and microstructure. It is noted that SLM is a rapid solidification process during which the interface is at the non-equilibrium state. Traditional phase-field models are usually based on the assumption of local equilibrium conditions at the interface. To simulate the non-equilibrium state of the interface during SLM process, a finite interface dissipation phase-field model (FIDPFM) [19–20] was selected, where interface permeability (P_I) was introduced to characterize the rate of solute transport across the phase interface. This approach allows effective description of the rapid solidification process through appropriate selection of P_I.

However, SLM involves multi-track scanning, leading to remelting phenomenon influenced by thermal history. Uddagiri et al[21] investigated the microstructural evolution of nickel-based alloys during solidification, remelting, and secondary solidification, highlighting the significant impact of remelting on microstructure morphology and solute distribution. Their simulation results were validated against experimental results of the Ni-20.5Al (mol%) binary alloy.

Currently, the research on SLM process of Ti-Nb alloys mainly concentrates on the adjustment and optimization of process parameters, such as laser power, scanning speed, and scanning strategy, to explore the relationship between process parameters and material properties. However, the effects of remelting due to multi-track scanning of SLM process on solidification microstructure have rarely been studied. In this research, based on the single-track scanning model, a dual-track scanning model was established, and the influence of remelting on the microstructure evolution of Ti-25Nb alloy during SLM process was examined. The simulations are expected to predict the effects of laser power, scanning speed, hatch spacing, and scanning directions on thermal history, molten pool morphology, and microstructural evolution.

2 Model Establishment

2.1 Temperature model, fluid flow model, and FIDPFM

Studying the temperature field (heat transfer field) and fluid flow field during the SLM process is crucial, and the key lies in establishing accurate heat transfer model and fluid flow model. A computational fluid dynamics (CFD) model was employed to clarify the processes, which includes the continuity equation[22], momentum equation[22], and energy equation[23]. For CFD model establishment and its details used in this research, equations from Ref. [16] are adopted. By solving those equations, accurate temperature field and fluid flow field of Ti-Nb alloy during the SLM process can be obtained.

Subsequently, the values of temperature gradient (G) and cooling rate (R_c) at the molten pool boundary were extracted and input into FIDPFM to study the solidification microstructure evolution. The details of governing equations for phase field and concentration field in FIDPFM are described in Ref. [18]. A two-dimensional simulation domain with an X-Z cross-sectional size of $128\Delta x \times 512\Delta z$ was used to study the impact of G and R_c on the solidification microstructure, and the actual size of the domain for phase-field simulation is 1.28 μm×5.12 μm. The initial setting of the simulation domain is as follows: a thin layer (with a thickness of $10\Delta x$) of β-phase at the left side, and a thick liquid phase at the right side. The method for the temperature changes within the simulation domain is described in Ref.[18].

To simulate the process of remelting and secondary solidification, the temperature for the second-track scanning is increased after the liquid phase has completely transformed into the solid phase for the first time (with the heating rate derived from the temperature field results), and the elevated temperature will hold until the complete remelting occurs. Subsequently, solidification is initiated again at 2075 K with new values of G and R_c.

2.2 Simulation parameters

In this research, commercial software Flow3D AM was used for simulation: a powder bed model was generated to solve the equations for heat transfer and fluid flow with the grid size of 6 μm. The simulation parameters used for CFD and phase-field simulations are listed in Ref.[18].

In order to investigate the effects of process parameters on the remelting of Ti-25Nb alloy during SLM process, the dual-track laser melting simulations were conducted using different laser powers (P), scanning speeds (V), hatch spacing (H), and scanning directions. For unidirectional scanning, the scanning

path is A-B-C-D, as shown in Fig. 1a. The laser starts to melt the powder from point A and then scans along the positive *X*-axis at a constant speed to point B. After the first track scanning, the laser moves to point C to start the second track scanning. During the second track scanning, the laser continues to scan from point C to point D along the positive *X*-axis, as shown in Fig. 1a. For zigzag scanning, the scanning path is A-B-D-C, as shown in Fig. 1b. The first track scanning is the same as the unidirectional scanning (from point A to point B). After the first track scanning, the laser moves to point D to start the second track scanning. During the second track scanning, the laser continues to scan from point D to point C along the negative *X*-axis, as shown in Fig. 1b.

The specific parameters used in these simulations are presented in Table 1. This approach allows for a comprehensive analysis of the influence of parameters on the remelting behavior, final solidification microstructure, and properties of the manufactured parts. According to the simulation results, valuable insights can be gained to optimize SLM process for Ti-Nb alloys.

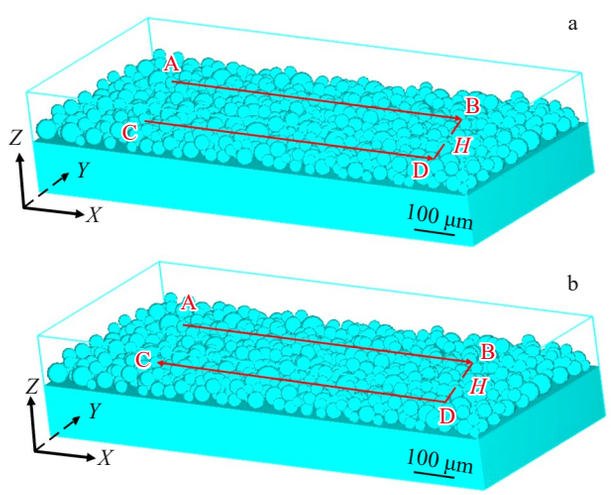

Fig. 1 Schematic diagrams of unidirectional scanning (a) and zigzag scanning (b) during SLM process

Table 1 Process parameters used for Flow3D AM simulations

Case	*P*/W	*V*/m·s^{-1}	*H*/μm	Scan direction
S1	120	0.50	80	Unidirectional
S2	150	0.50	80	Unidirectional
S3	180	0.50	80	Unidirectional
S4	150	1.00	80	Unidirectional
S5	150	0.75	80	Unidirectional
S6	150	0.50	80	Unidirectional
S7	150	0.50	70	Unidirectional
S8	150	0.50	60	Unidirectional
S9	150	0.50	80	Zigzag
S10	150	0.50	70	Zigzag
S11	150	0.50	60	Zigzag

3 Results

3.1 Molten pool and solidification microstructure under different laser powers

Laser power has a significant impact on the microstructure and properties of SLMed parts, particularly the molten pool temperature field and the microstructure at the molten pool boundary. Laser power of 120, 150, and 180 W were selected in this research.

Fig. 2 shows the molten pool morphology in the case of the single-track scanning with the process parameters of *P*=150 W, *V*=0.50 m/s, and *H*=80 μm. The upper and lower white dashed lines in Fig. 2 represent the centerlines of the top and bottom of the molten pool, respectively. As shown in Fig. 2, area A and area B represent the microzones for analysis at the top and bottom of the molten pool, respectively. The red areas indicate that the temperature of those parts of molten pool is above the melting point; the blue areas are related to the unmelted solid powder, solidified zone after melting, or substrate; other colors are related to the mushy zone.

Fig. 3 displays the morphologies of SLMed Ti-25Nb alloy after dual-track scanning under conditions of *V*=0.5 m/s, *H*=80 μm, and unidirectional mode. As shown in Fig. 3, the size of molten pool generally shows a positive linear relationship with the applied laser power. At lower laser power (120 W), a small molten pool is produced with the length of 180 μm and depth of 36 μm. At higher laser power (150 W), the molten pool has a length of 275 μm and a depth of 48 μm. The length and depth of the molten pool increase by 52.7% and 33.3%, compared with those at 120 W, respectively. When the applied laser power increases to 180 W, the molten pool has a length of 455 μm and a depth of 66.6 μm. Compared with those at 150 W, the length and depth of the molten pool increase by 65.4% and 38.75%, respectively. When *P*=180 W, the size of the molten pool significantly increases after dual-track scanning, indicating that at the laser power of 180 W, the thermal accumulation from the first track has a significant impact on the subsequent track.

Fig. 4 shows the temperature evolution at the top and bottom boundaries of the molten pool during dual-track scanning under conditions of *H*=80 μm, *V*=0.50 m/s, unidirectional mode, and different laser powers. The location data of the top boundary are *X*=0.500 mm, *Y*=0.240 mm, and *Z*=0.112 mm; the location data of the bottom boundary are

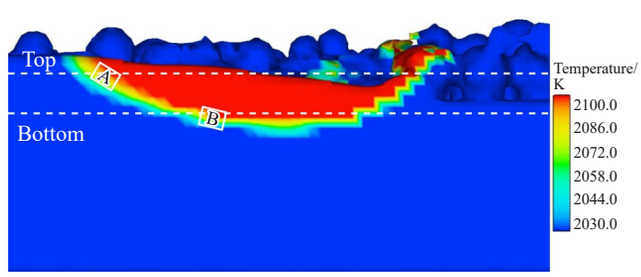

Fig. 2 Temperature distribution in molten pool of SLMed Ti-25Nb alloy during single-track scanning under conditions of *P*=150 W, *V*=0.50 m/s, and *H*=80 μm

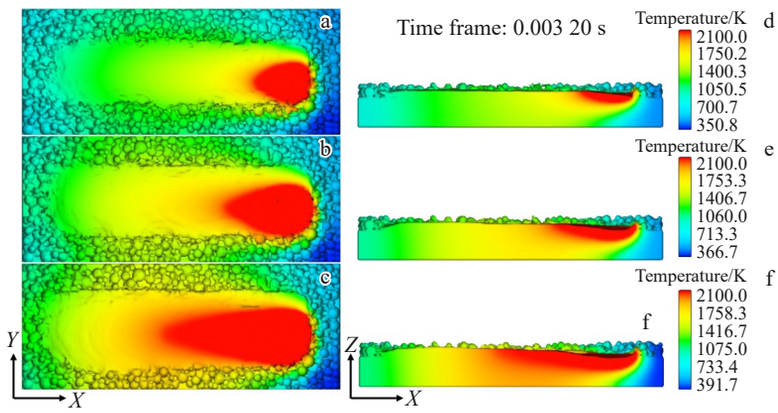

Fig.3 Top (a–c) and longitudinal (d–f) morphologies of SLMed Ti-25Nb alloy after dual-track scanning under conditions of H=80 μm, V=0.50 m/s, unidirectional mode, and different laser powers: (a, d) 120 W; (b, e) 150 W; (c, f) 180 W

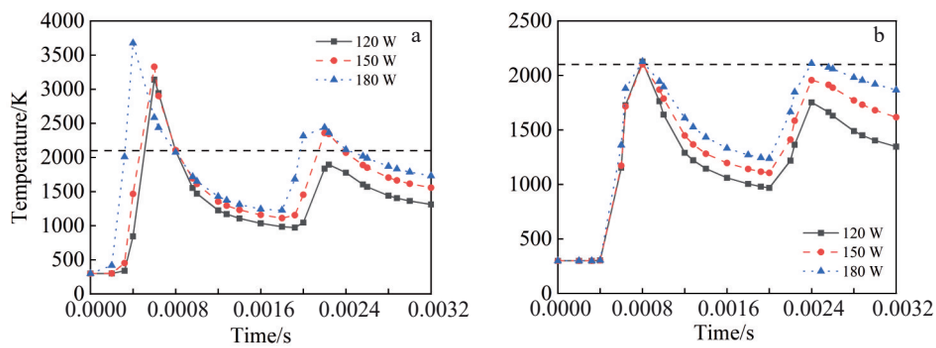

Fig.4 Temperature evolution at top (a) and bottom (b) boundaries of molten pool during dual-track scanning under conditions of H=80 μm, V=0.50 m/s, unidirectional mode, and different laser powers

X=0.500 mm, Y=0.240 mm, and Z=0.082 mm. The dashed line represents the liquidus temperature (2100 K). The temperature distribution curves at 2030 – 2100 K region and peak temperature region show linear fitting relationships, and the slopes of their fitted functions represent the minimum temperature gradient (G_{min}) and the maximum temperature gradient (G_{max}), respectively. The minimum cooling rate (R_{cmin}) and the maximum cooling rate (R_{cmax}) are obtained from the temperature cooling curves at 2030–2100 K region and peak temperature region, respectively[16]. In the subsequent phase-field simulations, the average values of G and R_c data were used for analysis. Fig. 4a shows that the second peak temperature exceeds the liquidus line under laser power of 150 and 180 W, indicating that remelting occurs under these conditions. However, the second peak temperature is below the liquidus line under laser power of 120 W. Therefore, the microstructure remains after the initial melting under laser power of 120 W. Fig. 4b shows that the second peak temperature exceeds the liquidus line only under the laser power of 180 W. This result indicates that the bottom of the first melt track is subjected to a lesser degree of thermal influence compared to the top area. After calculating G and R_c values, they are coupled with FIDPFM to obtain the microstructure at the top and bottom boundaries of the molten pool boundary.

Fig.5 depicts the solidification microstructures (represented by Nb content) at various heights along the molten pool boundary of SLMed Ti-25Nb alloy after dual-track scanning under conditions of H=80 μm, V=0.50 m/s, unidirectional mode, and different laser powers (120, 150, and 180 W). The location data of the top boundary are X=0.500 mm, Y=0.240 mm, and Z=0.112 mm; the location data of the bottom boundary are X=0.500 mm, Y=0.240 mm, and Z=0.082 mm. SD in Fig.5 represents the solidification direction. At the top area of molten pool boundary, remelting occurs under laser power of 150 and 180 W. Fig. 5a – 5b illustrate that the microstructure after remelting exhibits cellular growth. In contrast, the microstructure in non-remetling areas shows columnar growth (Fig.5c). Besides, the cellular dendritic size under laser power of 180 W is larger than that of 150 W. This is due to the increased energy density and the effect of thermal cycles, and this result is consistent with that from Ref.[24]. At the bottom area of the molten pool boundary, the remelted microstructure exhibits dendritic crystal growth (Fig. 5d), whereas the microstructure in the non-remelting areas shows cellular growth (Fig.5e–5f).

3.2 Molten pool and solidification microstructure under different laser velocities

Three laser velocities (V=0.50, 0.75, and 1.00 m/s) were selected for analysis. Fig. 6 displays the morphologies of SLMed Ti-25Nb alloy after dual-track scanning under

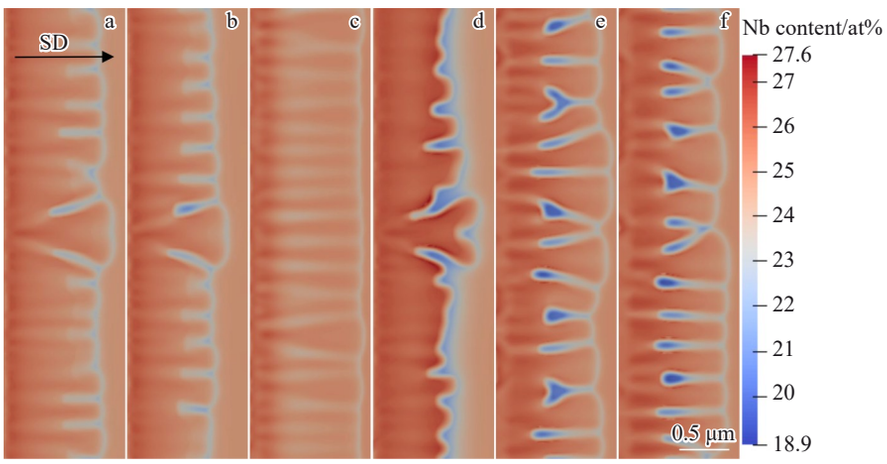

Fig.5 Solidification microstructures at top (a – c) and bottom (d – f) boundaries of molten pool after dual-track scanning under conditions of H=80 μm, V=0.50 m/s, unidirectional mode, and different laser powers: (a, d) 180 W; (b, e) 150 W; (c, f) 120 W

conditions of P=150 W, H=80 μm, unidirectional mode, and laser velocity of 0.50, 0.75, and 1.00 m/s. It can be seen that the dimensions of the molten pool have a negative linear relationship with the applied V condition. Besides, as V increases, the melt track becomes rougher and discontinuous. An increase in V results in a reduction of laser energy density. At the highest V of 1.00 m/s, a small molten pool is produced with a length of 171 μm and a depth of 30 μm. For the case with relatively lower V of 0.75 m/s, the molten pool has a length of 204 μm and a depth of 36 μm. The length and depth of the molten pool increase by 19.3% and 20.0%, compared with those obtained under V=1.00 m/s, respectively. When V decreases to 0.50 m/s, the molten pool has a length of 275 μm and a depth of 48 μm. Compared with those obtained under V=0.75 m/s, the length and depth of the molten pool increase by 34.8% and 33.3%, respectively. Compared with Fig. 5, the cross-section morphology of the molten pool is more sensitive to parameter P than parameter V, which is consistent with the results in Ref.[25].

Fig. 7 shows the temperature evolution at top and bottom boundaries of the molten pool during dual-track scanning under conditions of P=150 W, H=80 μm, unidirectional mode, and different laser velocities. The location data of the top boundary are X=0.500 mm, Y=0.240 mm, and Z=0.112 mm; the location data of the bottom boundary are X=0.500 mm, Y=0.240 mm, and Z=0.082 mm. Fig. 7a indicates that at laser velocity of 0.50 m/s, the second peak temperature exceeds the liquidus line, suggesting that remelting occurs. At V=0.75 and 1.00 m/s, the initial solidification microstructure retains. Fig. 7b shows that at the bottom boundary of molten pool, the second peak temperature is below the liquidus temperature under all velocity conditions.

Fig. 8 shows the solidification microstructures (represented by Nb content) at various heights along the molten pool boundary of SLMed Ti-25Nb alloy after dual-track scanning under conditions of P=150 W, H=80 μm, unidirectional mode, and different laser velocities (0.50, 0.75, and 1.00 m/s). SD in Fig. 8 represents the solidification direction. The location data of the top boundary are X=0.500 mm, Y=0.240 mm, and Z=0.112 mm; the location data of the bottom boundary are X=0.500 mm, Y=0.240 mm, and Z=0.082 mm. At the top of the molten pool boundary, remelting only occurs under the condition of V=0.50 m/s. Fig. 8a shows that the microstructure after remelting exhibits cellular growth. The microstructure is

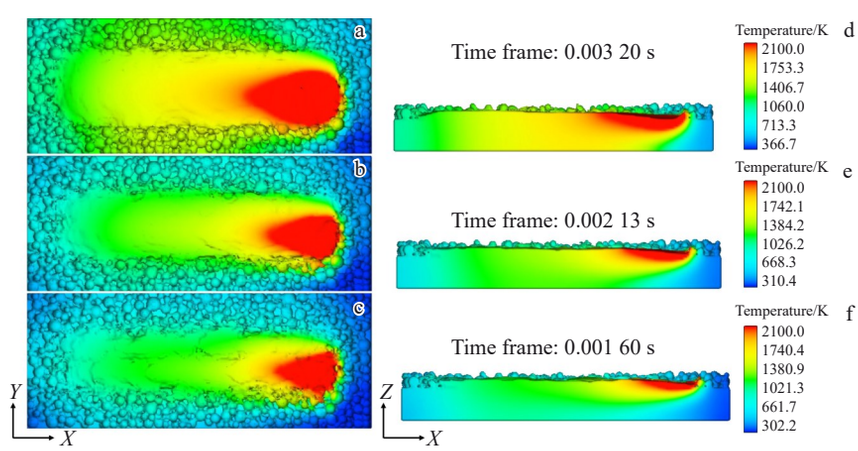

Fig.6 Top (a–c) and longitudinal (d–f) morphologies of SLMed Ti-25Nb alloy after dual-track scanning under conditions of P=150 W, H=80 μm, V=0.5 m/s, unidirectional mode, and different laser velocities: (a, d) 0.50 m/s; (b, e) 0.75 m/s; (c, f) 1.00 m/s

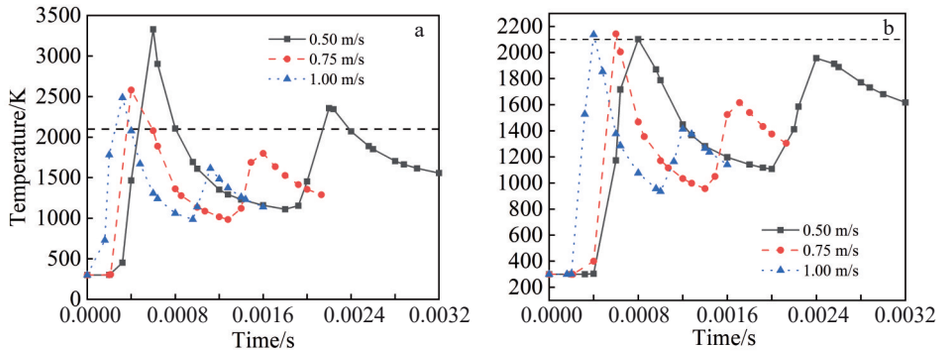

Fig.7 Temperature evolution at top (a) and bottom (b) boundaries of molten pool during dual-track scanning under conditions of P=150 W, H=80 μm, unidirectional mode, and different laser velocities

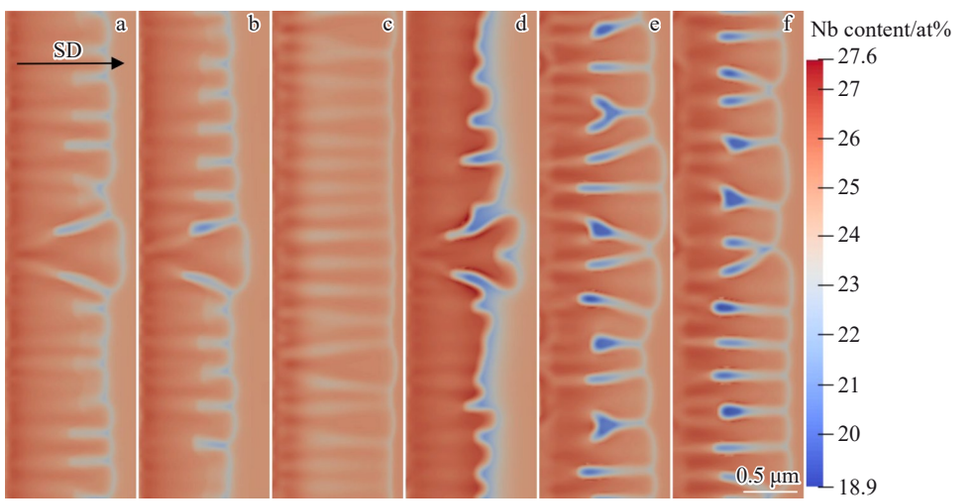

Fig.8 Solidification microstructures at top (a–c) and bottom (d–f) boundaries of molten pool boundary after dual-track scanning under conditions of P=150 W, H=80 μm, unidirectional mode, and different laser velocities: (a, d) 0.50 m/s; (b, e) 0.75 m/s; (c, f) 1.00 m/s

coarse cellular crystal under V=0.75 m/s and columnar crystal under V=1.00 m/s. It is noted that due to the occurrence of remelting under V=0.50 m/s, both the temperature gradient and the cooling rate decrease, resulting in cellular crystal growth. However, the temperature gradient under V=0.75 m/s is higher than that under V=0.5 m/s, and the microstructure is coarse cellular crystal. At the bottom boundary of the molten pool, no remelting occurs, and cellular crystal growth can be observed under all scanning speed conditions. It can be seen that as the scanning speed increases, the cellular crystal size decreases and it tends to grow in a planar pattern (Fig.8d–8f). This is because the increased scanning velocity leads to a faster cooling rate at the interface, which causes the interface morphology change from cellular type to columnar crystal growth, resulting in finer grains.

3.3 Molten pool and solidification microstructure under different scanning strategies

Hatch spacing, the distance between two neighboring scan paths, is regarded as an essential processing variable to control the porosity of SLMed samples. This is because pores are mainly caused by insufficient overlap[26]. However, the relationship between pore formation and overlap degree of stacking materials is intricate. It was found that when the laser power was below 150 W and the hatch spacing was 80 μm, the temperature at the centerline of the first track did not reach the melting point during the second track, thus failing to achieve remelting. Therefore, to ensure remelting, laser power of 150 W and scanning speed of 0.50 m/s were selected. With these parameters, hatch spacing of 60, 70, and 80 μm were used to study the influence of hatch spacing on temperature field and solidification microstructure.

Fig. 9 and Fig. 10 display the morphologies of SLMed Ti-25Nb alloy after dual-track scanning under conditions of varying hatching space, P=150 W, and V=0.50 m/s with unidirectional and zigzag scanning strategies, respectively. It can be seen that the molten pool has an irregular ellipse shape: a slender tail extends from the molten pool, and a shallow pit exists at the center. With the decrease in hatch spacing, the size of the molten pool is increased. This is because the smaller the hatch spacing, the greater the thermal accumulation during the heating of the first track. This phenomenon leads to a larger influence on the adjacent second track. Consequently, the temperature of the second track rises more quickly, and the peak temperature is also higher,

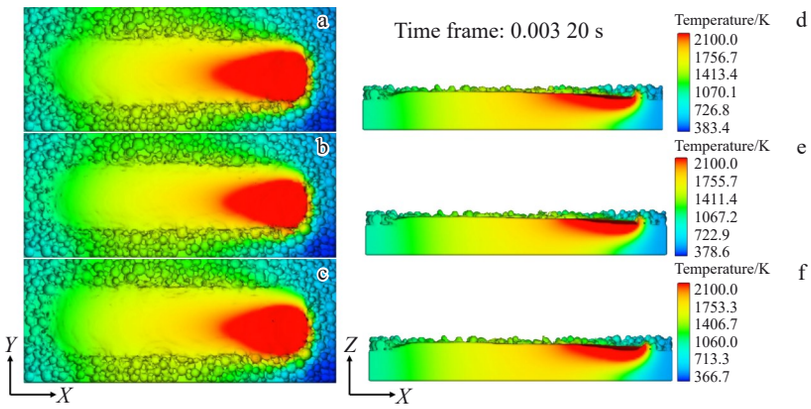

Fig.9 Top (a – c) and longitudinal (d – f) morphologies of SLMed Ti-25Nb alloy after dual-track scanning under conditions of P=150 W, V=0.50 m/s, unidirectional mode, and different hatching spacing: (a, d) 60 μm; (b, e) 70 μm; (c, f) 80 μm

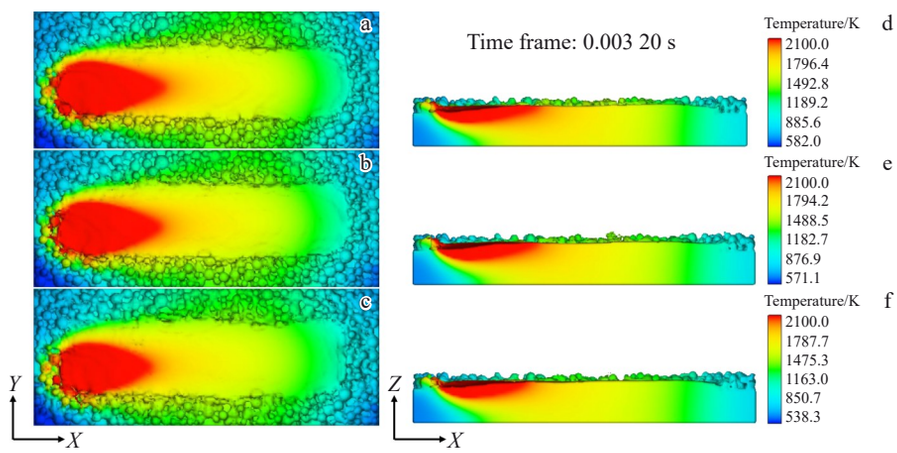

Fig.10 Top (a – c) and longitudinal (d – f) morphologies of SLMed Ti-25Nb alloy after dual-track scanning under conditions of P=150 W, V=0.50 m/s, zigzag mode, and different hatching spacing: (a, d) 60 μm; (b, e) 70 μm; (c, f) 80 μm

resulting in the formation of a larger molten pool. Additionally, it can be seen that changing scanning direction leads to the alteration in the direction of the molten pool.

Fig. 11 and Fig. 12 display the temperature evolution at the top and bottom boundaries of the molten pool after dual-track scanning with unidirectional and zigzag scanning strategies under conditions of varying hatching spacing, P=150 W, and V=0.50 m/s, respectively. The location data of the top boundary are X=0.500 mm, Y=0.240 mm, and Z=0.112 mm; the location data of the bottom boundary are X=0.500 mm, Y=0.240 mm, and Z=0.082 mm. As shown in Fig. 11, under both scanning strategies, the temperature rises sharply during the first track and then decreases gradually. When the second-track scanning begins, the temperature rises again. Additionally, the second peak temperature decreases. It is also noted that with the decrease in hatch spacing, the peak

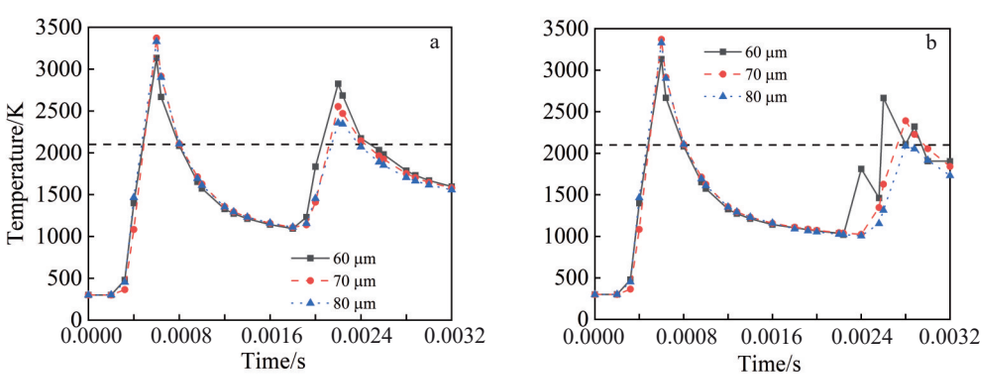

Fig.11 Temperature evolution at top boundary of molten pool during dual-track scanning with unidirectional mode (a) and zigzag mode (b) under conditions of P=150 W, V=0.50 m/s, and varying hatch spacing

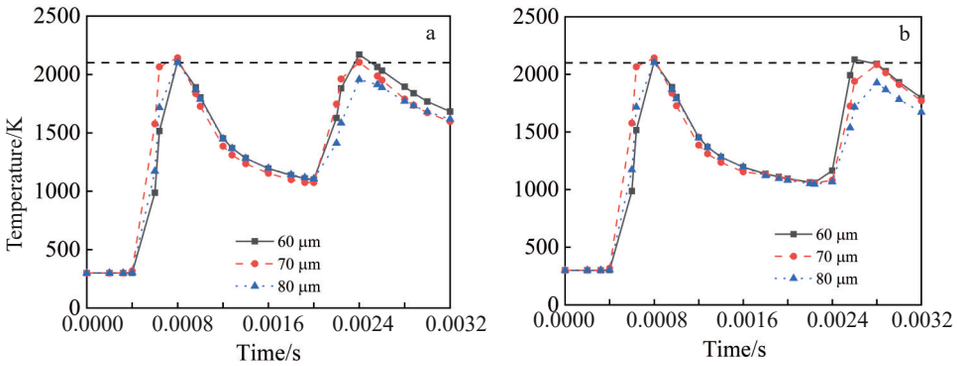

Fig.12 Temperature evolution at bottom boundary of molten pool during dual-track scanning with unidirectional mode (a) and zigzag mode (b) under conditions of P=150 W, V=0.50 m/s, and varying hatch spacing

temperature is increased. This is because a reduced hatch spacing leads to a greater thermal impact induced by the second track on the first track. Compared with that under zigzag mode, the initiation of temperature rise is early under unidirectional mode, and the second peak temperatures under all directions are above the liquidus line, indicating that remelting occurs. According to Fig. 12, the initiation of temperature rise is also early under unidirectional mode. However, with the unidirectional mode, the second peak temperatures are above the liquidus line when the hatch spacing is 60 and 70 μm, whereas with the zigzag mode, the second peak temperature is above the liquidus line only when the hatch spacing is 60 μm. This is attributed to the greater thermal influence induced by the second track on the first track during dual-track scanning with unidirectional mode. Therefore, the bottom of the molten pool of the first track remelts when the hatch spacing is 60 and 70 μm.

Fig. 13 and Fig. 14 depict the solidification microstructures (represented by Nb content) of SLMed Ti-25Nb alloy after dual-track scanning with unidirectional and zigzag scanning strategies under conditions of varying hatching space, P=150 W, and V=0.50 m/s, respectively. The location data of the top boundary are X=0.500 mm, Y=0.240 mm, and Z=0.112 mm; the location data of the bottom boundary are X=0.500 mm, Y=0.240 mm, and Z=0.082 mm. The black arrows in Fig. 13 and Fig. 14 indicate the solidification direction, namely SD. According to Fig. 13a–13c, at the top boundary of the molten pool, the remelted microstructure under condition of hatch spacing of 60 μm exhibits columnar crystals, while the microstructures under condition of hatch spacing of 80 and 70 μm show cellular crystals. Additionally, the dendrite size under condition of hatch spacing of 80 μm is smaller than that of 70 μm, which is consistent with the experimental results in Ref. [27]. It can be found that under the condition of hatch spacing of 80 μm (Fig. 13d), remelting does not occur at the bottom boundary of the molten pool, resulting in the formation of cellular structure, which is significantly different from the dendrites after remelting (Fig. 13e – 13f). Moreover, the cellular size under the condition of hatch spacing of 70 μm is larger than that of 60 μm. It should be noted that with the zigzag scanning strategy, due to the opposite scanning directions of the first and second tracks, the growth direction

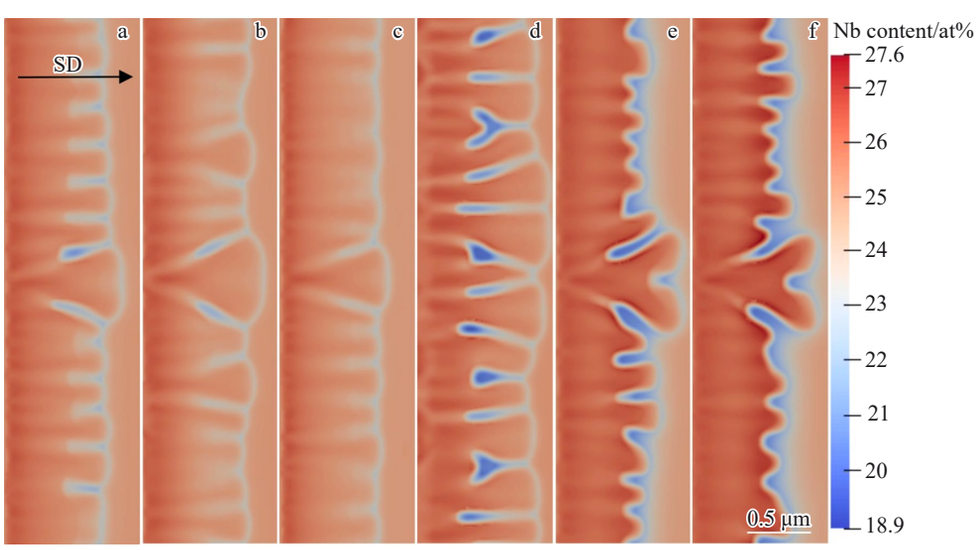

Fig.13 Solidification microstructures at top (a–c) and bottom (d–f) boundaries of molten pool after dual-track scanning with unidirectional mode under conditions of P=150 W, V=0.50 m/s, and varying hatch spacing: (a, d) 80 μm; (b, e) 70 μm; (c, f) 60 μm

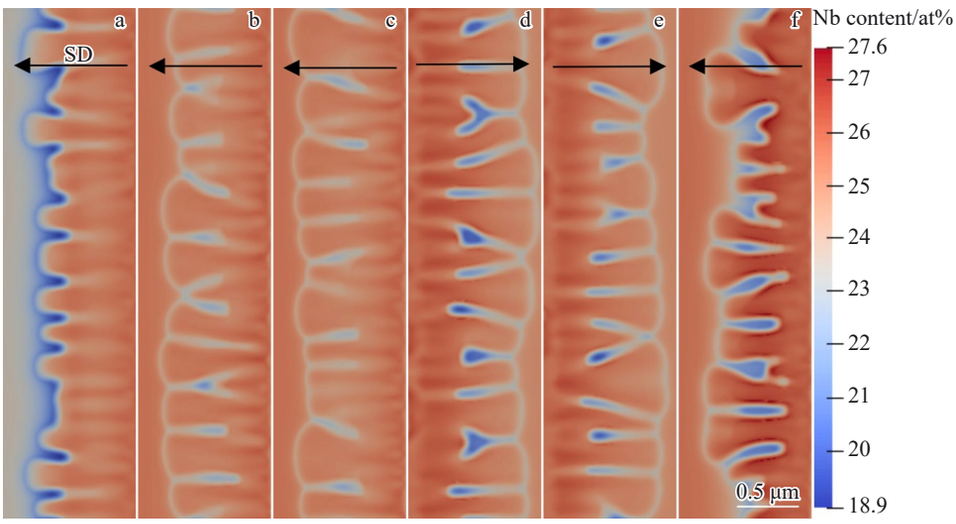

Fig.14 Solidification microstructures at top (a–c) and bottom (d–f) boundaries of molten pool after dual-track scanning with zigzag mode under conditions of P=150 W, V=0.50 m/s, and varying hatch spacing: (a, d) 80 μm; (b, e) 70 μm; (c, f) 60 μm

of the recrystallized grains changes. For example, under the condition of hatch spacing of 80 and 70 μm (Fig. 14d–14e), remelting does not occur at the bottom boundary of the molten pool. It is found that the microstructure size after dual-track scanning with zigzag mode is larger than that with unidirectional mode.

4 Discussion

4.1 Evolution mechanisms of temperature gradient and cooling rate

To elucidate the evolution mechanisms of cooling rate and temperature gradient during the rapid heating and solidification processes of Ti-Nb alloy fabricated by SLM, a comprehensive relationship among SLM process, thermal conductivity, and heat radiation/convection of the Ti-Nb alloy was established. The temperature gradient (G), as the temperature difference between two measurement points within a certain distance, is determined by two factors: the difference in energy input and the difference in heat transfer capability between these two measurement points. In this research, the laser heat source conforms to a Gaussian distribution, leading to the highest energy input at the central point with a gradual decrease to the minimum value on both sides. As a result, different energy inputs exist between the two measurement points. Moreover, due to the weak thermal conductivity (27 $W\cdot(m\cdot K)^{-1}$ at 1900 K) of Ti-Nb alloy, the temperature difference between measurement points will be large, thereby creating a high-temperature gradient. During the rapid solidification process, the molten pool has an extremely fast cooling rate due to the combined effects of the thermal conductivity within the molten pool and the heat convection/radiation on the molten pool surface. It is believed that the grain growth is determined by the G value that determines the grain growth direction and the R_c value that determines the grain size[28]. According to the crystallization theory, each crystal structure has its unique preferred crystal orientation, and both G and R_c play important roles in influencing the crystal growth rate.

Since SLM is a complex thermal process involving rapid heating and cooling, the temperature gradient and cooling rate of the molten pool will change with each laser scanning. Use cases S3 and S11 (Table 1) as examples for validation, because both groups undergo remelting at the top and bottom of molten pool, indicating that resolidification occurs in both cases. This enables the changes in G and R_c at the top and bottom boundaries of the molten pool during the dual-track process. Fig. 15 depicts the variations of G and R_c in cases S3 and S11 during the dual-track scanning process. It is clear that the G and R_c at the bottom boundary of molten pool are different from those at the top boundary. As for case S3, the maximum temperature gradient of the molten pool reaches 6.685 K/μm, which is significantly higher than that at the bottom boundary (2.475 K/μm). Meanwhile, the cooling rate of the molten pool changes from 3.045 K/s to 1.140 K/s. Such significant variation in temperature gradient and cooling rate may form a gradient microstructure in SLMed part. According to Fig. 5 and Fig. 13, it can be inferred that the top surface exhibits the highest microhardness with fine cellular and columnar dendrites. At the bottom boundary of the molten pool, typical dendrites with larger grain sizes can be observed. The simulated gradient microstructure is consistent with the typical gradient microstructure observed in experiments[28].

4.2 Formation mechanisms of solidification microstructure

Generally, the development of solidification microstructure is determined by two factors: the temperature gradient (G) and the solidification rate (R), where the latter is defined as the propagation speed of the solid-liquid interface[27]. The propagation speed of the solid-liquid interface is also denoted as V_I. The combination of these two factors influences the final microstructure. The ratio of these two parameters (G/R) determines the solidification microstructure. The molten pool

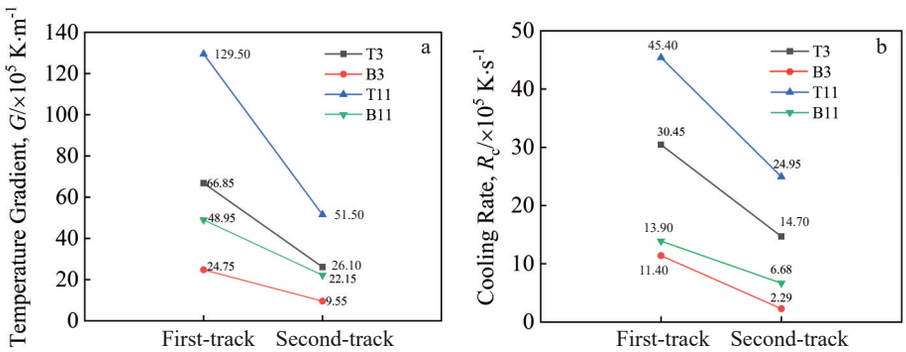

Fig.15 Variations of temperature gradient G (a) and cooling rate R_c (b) at top and bottom boundaries of molten pool in cases S3 and S11 during dual-track scanning process (T3 and B3 represent the top and bottom boundaries in case S3, respectively; T11 and B11 represent the top and bottom boundaries in case S11, respectively)

can be divided into several regions with different microstructures, such as columnar dendrites with single grain growth direction or multiple grain growth directions, cellular dendrites, and equiaxed grains[26]. The cooling rate R_c=GR, which affects the microstructure size. Moreover, G and R_c are of utmost importance to the determination of V_I. According to the interface morphological stability theory[27], as V_I increases, the interface morphology changes according to the sequence of planar-cellular-dendritic-cellular-planar structures[28]. The solidification morphology is determined by solute diffusion and interfacial tension. At low V_I, solute diffusion plays a significant role in the formation of columnar or cellular structures. At high V_I, the primary dendrite arm spacing (PDAS) and the radius at the dendrite tip decrease, which restricts the formation of dendrites and even cellular structures, leading to the formation of a planar interface. It is found that the smaller the R_c value and the larger the G value, the larger the V_I value[18].

Fig. 16 shows the solidification morphology selection map for Ti-25Nb alloy, demonstrating the variation in the morphology and size of cellular segregation structure as a function of G and R. With the selected alloy composition, three types of growth morphologies, i.e., planar, cellular, and dendritic structures, after SLM process with varying process parameters are predicted. Fig. 16 is based on the microstructure simulations under different G and R conditions. The predicted growth morphologies for each GR combination (such as dendritic crystals, cellular structures, and planar growth) are also presented in Fig. 16. Then, the boundaries of the microstructure morphologies are roughly determined. From the bottom left corner to the middle area in Fig. 16, a transition from dendrites to cellular structure and then to planar structure can be observed. In addition to the types of microstructures, the solidification map can also be used to obtain the variation of cell size (such as PDAS) with G and R. It should be noted that PDAS is obtained by dividing the size of the simulation domain through the number of primary dendrites in the simulation domain. However, it is difficult to calculate the number of primary dendrites for dendrites crystals. Therefore, PDAS can only be calculated when there

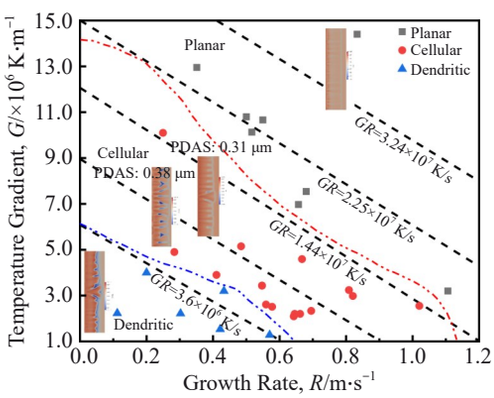

Fig.16 Variations in solidification morphology, size of cellular segregation structure (PDAS), and micro-segregation as a function of growth rate and temperature gradient for SLMed Ti-25Nb alloy

are cellular crystal growth. According to Fig. 16, it can be known that with the increase in cooling rate (from the bottom left corner to the top right corner), PDAS becomes smaller, or the cell becomes finer. The boundary morphologies of the planar and cellular microstructures, as well as the trends in grain size variation, are similar to the solidification morphologies from the selection map of the Ti-Nb alloy[23].

Once remelting occurs, both G and R_c decrease. Therefore, to explore the formation mechanism of the resolidification microstructure at the molten pool boundary, the changes in the microstructure before and after remelting should be investigated. Fig. 17 depicts the solidification microstructure at the top boundary of the molten pool before and after remelting in cases S3, S6, and S11 (the black arrows indicate the solidification direction, namely SD). It can be observed that during the first solidification, the microstructures in Fig. 17a–17b exhibit columnar dendrites, while the microstructure in Fig. 17c shows a cellular grain morphology. This is consistent with the experimental results in Ref. [26]. Additionally, the dendrite size in Fig. 17c is noticeably larger. This phenomenon indicates that the V_I value in case S6 is greater than that in case S11. Thus, with the decrease in hatch spacing, V_I is

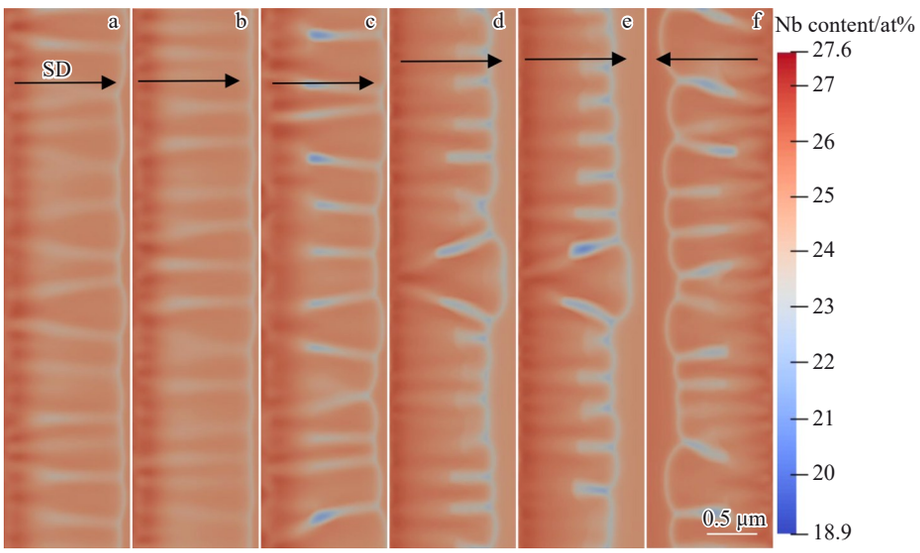

Fig.17 Solidification microstructures at top boundary of molten pool of Ti-25Nb alloy in different cases before (a–c) and after (d–f) remelting during the dual-track scanning process: (a, d) case S3; (b, e) case S6; (c, f) case S11

decreased. Comparing the solidification microstructures from the first solidification before remelting (Fig. 17a–17c) and the second solidification after remelting (Fig. 17d–17f), it can be observed that the solidification microstructure changes from columnar type into cellular type after remelting, and the dendrite size increases. Ti-6Al-4V alloy was observed by scanning electron microscope (SEM), and its morphologies after remelting are shown in Fig. 18[31]. Ti-Nb alloy before and after remelting was also investigated using SEM coupled with energy dispersive spectrometer (EDS), and results are shown in Table 2[32] and Fig. 19[32]. The experimental results indicate that due to the influence of thermal accumulation, the grain size increases after remelting. Furthermore, with the decrease in hatch spacing or the increase in energy density, the thermal accumulation is greater, and the grain size becomes larger. According to the interface morphological stability theory, it can infer that the V_I during the second solidification is slower than that during the first solidification. Because both G and R_c decrease after remelting, considering the negative correlation between G and V_I and the positive correlation between R_c and V_I, it can be concluded that V_I is more sensitive to the decrease in R_c after remelting. Comparing Fig. 17c and 17f, it can be seen that with the zigzag scanning strategy, the microstructure growth direction is opposite after remelting. As a result, the grain growth directions in the remelted area and the adjacent un-remelted area will influence each other. This may be the

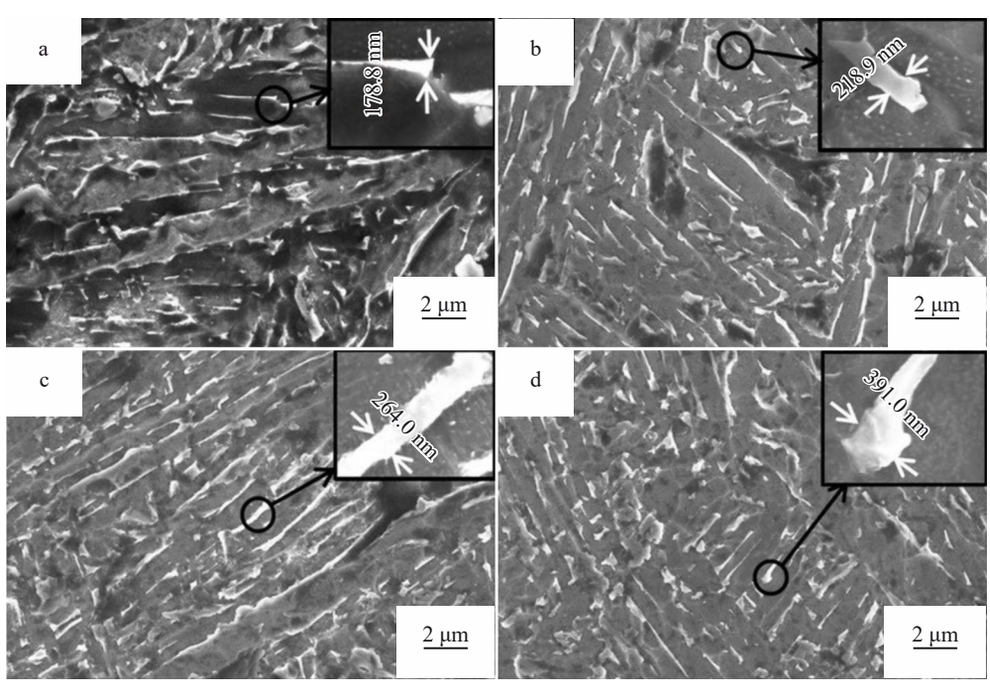

Fig.18 SEM images of Ti-6Al-4V alloy processed by SLM with different overlapping ratios after remelting[31]: (a) 4%; (b) 20%; (c) 36%; (d) 52%

Table 2 EDS analysis results of Ti-Nb alloy before and after remelting (wt%)[32]

State	Ti content	Nb content
Before remelting	55.3	44.7
After remelting	54.2	45.8

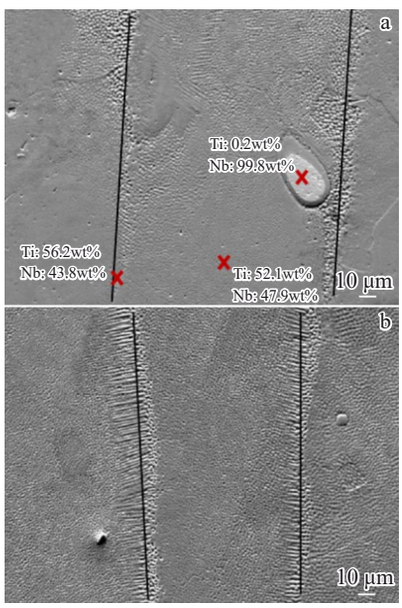

Fig.19 SEM images of Ti-Nb alloy before (a) and after (b) remelting[32]

reason why the zigzag scanning strategy leads to higher density, higher microhardness, and lower residual stress[30].

5 Conclusions

A multi-physics approach is employed to investigate the remelting and solidification of Ti-25Nb (at%) alloy during the dual-track SLM process. The influence laws and mechanisms of several factors are obtained.

1) Laser power: the solidification process is significantly influenced by laser power. Higher laser powers enhance thermal accumulation since the first track, leading to larger melt tracks and molten pool sizes. For example, under laser power of 150 W, the molten pool length increases by 52.7%, compared with that under laser power of 120 W. Remelting occurs at the top boundary of the molten pool under laser powers of 150 and 180 W; at the bottom boundary, remelting only occurs under laser power of 180 W. The remelting results in coarser grains, and it changes the growth pattern from cellular type to dendritic type due to decreased interface velocity.

2) Scanning speed: increasing scanning speed can reduce thermal accumulation since the first track, leading to rougher melt tracks and smaller molten pools. For instance, under scanning speed of 0.75 m/s, the molten pool length increases by 19.3%, compared with that under scanning speed of 1.00 m/s. Remelting at the top boundary of the molten pool only occurs under the scanning speed of 0.50 m/s, and it does not occur at the bottom boundary under any speed. After remelting of the top area, grains are coarser with a cellular growth pattern, while the bottom area retains the refined grain structure with the increase in scanning speed.

3) Hatch spacing: larger hatch spacing can roughen the melt track and reduce molten pool size. Remelting occurs under all conditions at the top boundary of molten pool. However, at the bottom boundary, it only occurs under conditions of unidirectional mode with hatch spacing of 60 and 70 μm, as well as zigzag mode with hatch spacing of 60 μm. The remelting leads to the dendritic growth.

4) Scanning strategy: the zigzag scanning strategy reverses the growth direction after remelting. As a result, the grain growth directions in the remelted area and the adjacent un-remelted area will influence each other, leading to better mechanical properties of processed parts.

5) Cooling rate and temperature gradient: at the molten pool boundary, both the cooling rate and the temperature gradient decrease. The interface velocity is particularly sensitive to these changes. According to interface morphological stability theory, remelting leads to the microstructure changes among planar, cellular, and dendritic growth patterns.

References

1 Liu S, Shin Y C. *Materials & Design*[J], 2019, 164: 107552
2 Xiao B, Jia W P, Wang J *et al*. *Rare Metal Materials and Engineering*[J], 2023, 52(9): 3056
3 DebRoy T, Wei H L, Zuback J S *et al*. *Progress in Materials Science*[J], 2018, 92: 112
4 Tshephe T S, Akinwamide S O, Olevsky E *et al*. *Heliyon*[J], 2022, 8(3): e09041
5 Yap C Y, Chua C K, Dong Z L *et al*. *Applied Physics Reviews*[J], 2015, 2(4): 041101
6 Davoodi E, Montazerian H, Mirhakimi A S *et al*. *Bioactive Materials*[J], 2022, 15: 214
7 Ma Yifan, Fan Jiangkun, Tang Luyao *et al*. *Rare Metal Materials and Engineering*[J], 2025, 54(1): 280 (in Chinese)
8 Hariharan A, Goldberg P, Gustmann T *et al*. *Materials & Design*[J], 2022, 217: 110618
9 Kaur M, Singh K. *Materials Science and Engineering C*[J], 2019, 102: 844
10 Qian M, Xu W, Brandt M *et al*. *MRS Bulletin*[J], 2016, 41(10): 775
11 Qin P, Chen L Y, Zhao C H *et al*. *Corrosion Science*[J], 2021, 189: 109609
12 Wang Z, Tan Y N, Li N. *Journal of Alloys and Compounds*[J], 2023, 965: 171030
13 Wang Q, Han C J, Choma T *et al*. *Materials & Design*[J], 2017, 126: 268
14 Wang J C, Liu Y J, Qin P *et al*. *Materials Science and Engineering A*[J], 2019, 760: 214
15 Liu Y L, Wang G, Zeng D C. *Modelling and Simulation in Materials Science and Engineering*[J], 2020, 28(6): 065004
16 Wang J C, Liu Y J, Rabadia C D *et al*. *Journal of Materials*

Science & Technology[J], 2021, 61: 221
17 Heo T W, Khairallah S A, Shi R P *et al*. *Journal of Physics: Materials*[J], 2021, 4(3): 034012
18 Cheng Y F, Wang G, Qiu Z G *et al*. *Acta Materialia*[J], 2024, 272: 119923
19 Zhang L J, Steinbach I. *Acta Materialia*[J], 2012, 60(6–7): 2702
20 Steinbach I, Zhang L J, Plapp M. *Acta Materialia*[J], 2012, 60(6–7): 2689
21 Uddagiri M, Shchyglo O, Steinbach I *et al*. *Metallurgical and Materials Transactions A*[J], 2023, 54(5): 1825
22 Yan W T, Ge W J, Qian Y *et al*. *Acta Materialia*[J], 2017, 134: 324
23 Karayagiz K, Johnson L, Seede R *et al*. *Acta Materialia*[J], 2020, 185: 320
24 Xue A T, Lin X, Wang L L *et al*. *Scripta Materialia*[J], 2021, 205: 114180
25 Li Y L, Gu D D. *Materials & Design*[J], 2014, 63: 856
26 Chen Y, Chen H, Chen J Q *et al*. *Journal of Manufacturing Processes*[J], 2020, 57: 533
27 Yang J J, Yu H C, Yin J *et al*. *Materials & Design*[J], 2016, 108: 308
28 Gu D D, Shi Q M, Lin K J *et al*. *Additive Manufacturing*[J], 2018, 22: 265
29 Chandra S, Radhakrishnan J, Huang S *et al*. *Progress in Materials Science*[J], 2025, 148: 101361
30 Jia H L, Sun H, Wang H Z *et al*. *The International Journal of Advanced Manufacturing Technology*[J], 2021, 113(9–10): 2413
31 Wang Q P, Kong J, Liu X K *et al*. *Advanced Engineering Materials*[J], 2021, 24(3): 2100876
32 Huang S, Sing S L, Yeong W Y. *Key Engineering Materials*[J], 2021, 24(3): 270

钛-铌合金激光选区熔化双道扫描过程中热历史对非平衡凝固组织影响的多物理场研究

吴　丹[1]，王　刚[1]，施荣沛[2]
(1. 华南理工大学 材料科学与工程学院，广东 广州 510641)
(2. 哈尔滨工业大学（深圳） 材料科学与工程学院，广东 深圳 518055)

摘　要：通过多物理场方法来量化工艺参数（激光功率、扫描速度、扫描间距和扫描策略）的变化对Ti-25Nb（原子分数）合金激光选区熔化（SLM）双道扫描过程的热历史以及相应的显微组织演变的影响。模拟结果表明，在双道扫描下，提高激光功率会形成更大的热积累，从而导致重熔时熔池体积增大和晶粒变粗。降低扫描速度会增强重熔，并促进熔池顶部的胞状晶生长，而更快的扫描速度会产生更粗糙的熔体轨迹和更细小的晶粒。扫描间距显著影响熔池尺寸和显微组织形态，较小的扫描间距有助于重熔。此外，采用往复式扫描时，第二熔道中晶粒的取向与第一熔道中的取向明显不同。更重要的是，与第一道次扫描相比，第二道次扫描后重熔熔池边界处的温度梯度和冷却速率都降低了，导致界面速度降低，凝固微观结构发生了显著变化。本研究为非平衡凝固组织调控提供了理论基础，并为钛合金的SLM工艺参数优化提供了新的见解。

关键词：激光选区熔化；非平衡凝固；热历史；有限界面耗散相场模型；显微组织演化

作者简介：吴　丹，男，1999年生，硕士，华南理工大学材料科学与工程学院，广东 广州 510641，E-mail：724116357@qq.com